A non-homogeneous Riemann solver for shallow water equations in porous media

F. Benkhaldoun[a], I. Elmahi[b], A. Moumna[b] and M. Seaid[c*]

[a] LAGA, Université Paris 13, 99 Av J.B. Clement, 93430 Villetaneuse, France; [b]ENSAO, EMSN, Complexe universitaire, BP 669, 60000 Oujda, Morocco; [c]School of Engineering and Computing Sciences, University of Durham, South Road, Durham DH1 3LE

The purpose of the current research is to develop an accurate and efficient solver for shallow water flows in porous media. The hydraulics is modeled by the two-dimensional shallow water flows with variable horizontal porosity. The variation of porosity in the water flows can be attributed to the variation of bed properties of the water system. As an example of porous shallow water flows is the passage of water discharge over vegetated areas in a river. Driving force of the phase separation and the mixing is the gradient of the porosity. For the numerical solution procedure we propose a non-homogeneous Riemann solver in the finite volume framework. The proposed method consists of a predictor stage for the discretization of gradient terms and a corrector stage for the treatment of source terms. The gradient fluxes are discretized using a modified Roe's scheme using the sign of the Jacobian matrix in the coupled system. A well-balanced discretization is used for the treatment of source terms. The efficiency of the solver is evaluated by several test problems for shallow water flows in porous media. The numerical results demonstrate high resolution of the proposed non-homogeneous Riemann solver and confirm its capability to provide accurate simulations for porous shallow water equations under flow regimes with strong shocks.

Keywords: Shallow water equations; porous media; finite volume method; unstructured grids; Riemann solver

AMS Subject Classifications: 76S99; 35L65; 65M08

1. Introduction

Mathematical modelling of shallow water flows in porous media is based on the formulation and solution of the appropriate equations of continuity and motion of water height and porosity. In general, hydrodynamical flows represent a three-dimensional turbulent Newtonian flow in complicated geometrical domains. The cost of incorporating three-dimensional data in natural water courses is often excessively high. Computational efforts needed to simulate three-dimensional turbulent flows can also be significant. In view of such considerations, many researchers have tended to use rational approximations in order to develop two-dimensional hydrodynamical models for water flows. Indeed, under the influence of gravity, many free-surface water flows can be modeled by the shallow water equations with the assumption that the vertical scale is much smaller than any typical horizontal scale. These equations can be derived from the depth-averaged incompressible Navier-Stokes equations using appropriate free-surface and boundary conditions along with a hydrostatic pressure assumption. The shallow water equations in

---

depth-averaged form have been successfully applied to many engineering problems and their application fields include a wide spectrum of phenomena other than water waves. For instance, the shallow water equations have applications in environmental and hydraulic engineering such as tidal flows in an estuary or coastal regions, rivers, reservoir and open channel flows, see [1, 8, 20] among others. In general, porous shallow water flows are determined by the characteristics of the hydraulic flow and the properties of the bed topography. Thus, dynamics of the water and dynamics of the bedload must be studied using a mathematical model accounting for porosity effects on the hydraulics. The model presented in this study solves the shallow water equations with variable porosity. Similar free-surface flow models have been developed in [10, 19] and the references therein. Applications of shallow water flows with porosity have also been studied in [7, 9, 11, 13, 14, 22, 23] among others. The governing equations form a two-dimensional nonlinear system of hyperbolic conservation laws with source terms. Such practical hydrodynamical problems are not trivial to simulate since the geometry can be complex and the topography irregular. Special attention has been given to the treatment of the source terms in shallow water flows on non-fat beds. It is well known that shallow water equations on nonflat topography have steady-state solutions in which the flux gradients are nonzero but exactly balanced by the source terms. This well-balanced concept is also known by conservation property (C-property), compare [3, 21] among others. One requirement for solving shallow water equations with porosity is that the numerical solver considered must conserve the C-property. It should also stressed that this C-property can be interpreted as a particular case of the general well-balancedness property in shallow water flows, see [12] for more details.

Nowadays, much effort has been devoted to develop numerical schemes for hydraulics models able to resolve all hydrodynamical scales. The well-established Roe's scheme [17] has been modified in [7] for the shallow water equations with porosity. However, for practical applications, this method may become computationally demanding due to its treatment of the source terms. Numerical methods based on approximate-state Riemann solvers have also been applied to shallow water equations with porosity in [9, 11]. Unfortunately, most HLLC solvers that solves real models correctly are still very computationally expensive. Recently, a modified Rusanov method has also been applied to shallow water equations with porosity in [14]. It is well known that Rusanov-type schemes do not solve Riemann problems but the numerical dissipation in the results obtained using these methods is very noticeable. In the current study, a class of finite volume methods is proposed for numerical simulation of transient flows involving porosity variations. The method consists of a predictor stage where the numerical fluxes are constructed and a corrector stage to recover the conservation equations. The sign matrix of the Jacobian matrix is used in the reconstruction of the numerical fluxes. Most of these techniques have been recently investigated in [2–5, 18] for solving the canonical shallow water models without accounting for porosity variation. The current study presents an extension of this method to transient flows involving porosity variation in the water flows. A detailed formulation of the sign matrix and the numerical fluxes is presented. The proposed method satisfies the property of well-balancing flux-gradient and source-term in the system. Numerical results will be shown for several shallow water problems in porous media.

The organization of this paper is as follows. In section 2 we present the governing equations for the two-dimensional shallow water equations in porous media. The finite volume method is formulated in section 3. This section includes both the dis-

cretization of gradient fluxes and the treatment of source terms. Section 4 contains numerical results and applications. Conclusions are summarized in section 5.

2. Equations for shallow water equations in porous media

In the present study, the governing equations represent depth-averaged mass and momentum conservation of a water in horizontal or/and vertical directions with porosity. These equations consist of the conservation of mass and momentum balance

$$\frac{\partial(\phi h)}{\partial t} + \frac{\partial}{\partial x}(\phi h u) + \frac{\partial}{\partial y}(\phi h v) = 0,$$

$$\frac{\partial}{\partial t}(\phi h u) + \frac{\partial}{\partial x}\left(\phi h u^2 + \frac{1}{2}g\phi h^2\right) + \frac{\partial}{\partial y}(\phi h u v) = -g\phi h \frac{\partial Z}{\partial x} + \frac{1}{2}gh^2\frac{\partial \phi}{\partial x}, \quad (1)$$

$$\frac{\partial}{\partial t}(\phi h v) + \frac{\partial}{\partial x}(\phi h u v) + \frac{\partial}{\partial y}\left(\phi h v^2 + \frac{1}{2}g\phi h^2\right) = -g\phi h \frac{\partial Z}{\partial y} + \frac{1}{2}gh^2\frac{\partial \phi}{\partial y},$$

where t is the time variable, $\mathbf{x} = (x, y)^T$ the space coordinates, $\mathbf{u} = (u, v)^T$ the depth-averaged water velocity, h the water depth, Z the bottom topography, g the gravitational acceleration and ϕ the porosity. Note that diffusion effects, Coriolis forces, bed and wind frictions have been neglected in the above system (1). It should also be stressed that for a constant porosity ϕ, the above equations reduce to the standard shallow water equations widely investigated in the literature, see for example [1, 3]. In the current work, we assume that the porosity depends on space variables, *i.e.*, $\phi = \phi(x, y)$.

For simplicity in the presentation, let us rewrite the equations (1) in the following vector form

$$\frac{\partial \mathbf{W}}{\partial t} + \frac{\partial \mathbf{F}(\mathbf{W})}{\partial x} + \frac{\partial \mathbf{G}(\mathbf{W})}{\partial y} = \mathbf{S}(\mathbf{W}), \quad (2)$$

where $\mathbf{W}$ is the vector of conserved variables, $\mathbf{F}$ and $\mathbf{G}$ are respectively, the physical fluxes in x- and y-direction, and $\mathbf{S}$ is the source term. These variables are defined as

$$\mathbf{W} = \begin{pmatrix} \phi h \\ \phi h u \\ \phi h v \end{pmatrix}, \qquad \mathbf{F}(\mathbf{W}) = \begin{pmatrix} \phi h u \\ \phi h u^2 + \frac{1}{2}g\phi h^2 \\ \phi h u v \end{pmatrix},$$

$$\mathbf{G}(\mathbf{W}) = \begin{pmatrix} \phi h v \\ \phi h u v \\ \phi h v^2 + \frac{1}{2}g\phi h^2 \end{pmatrix}, \qquad \mathbf{S}(\mathbf{W}) = \begin{pmatrix} 0 \\ -g\phi h \frac{\partial Z}{\partial x} + \frac{1}{2}gh^2\frac{\partial \phi}{\partial x} \\ -g\phi h \frac{\partial Z}{\partial y} + \frac{1}{2}gh^2\frac{\partial \phi}{\partial y} \end{pmatrix}.$$

Note that the equations (2) have to be solved in a bounded spatial domain Ω
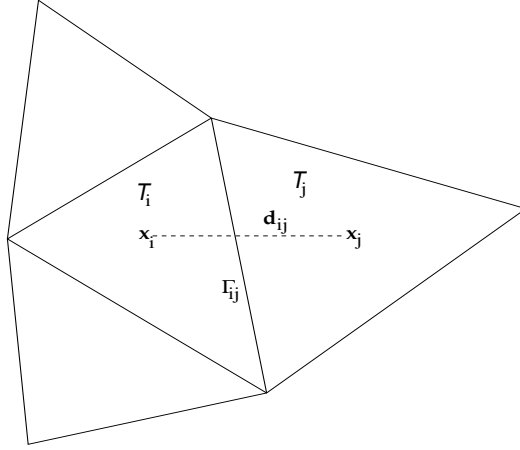
3

Figure 1. A generic control volume and notations.

with smooth boundary Γ, equipped with given boundary and initial conditions. In practice, these conditions are problem dependent and their discussion is postponed for section 4 where numerical examples are discussed. In addition, the topography and porosity variables in the system (2) are assumed to be well-defined as analytical functions of x and y or given data to be used in the numerical solver.

3. Unstructured Non-homogeneous Riemann Solver

The governing equations (2) are formulated in the Cartesian coordinates and will be discretized into the unstructured grids by the finite volume method. The unstructured grids are polygons and the number of edges of the grids is not limited in theory, but only triangular grids are considered in the current study. Hence, we divide the time interval into sub-intervals $[t_n, t_{n+1}]$ with stepsize Δt and discretize the spatial domain $\Omega \cup \Gamma$ in conforming triangular elements $\mathcal{T}_i$. Each triangle represents a control volume and the variables are located at the geometric centers of the cells. Hence, using the control volume depicted in Figure 1, a finite volume discretization of (2) yields

$$\mathbf{W}_i^{n+1} = \mathbf{W}_i^n - \frac{\Delta t}{|\mathcal{T}_i|} \sum_{j \in N(i)} \int_{\Gamma_{ij}} \mathcal{F}(\mathbf{W}^n; \mathbf{n}) \, d\sigma + \frac{\Delta t}{|\mathcal{T}_i|} \int_{\mathcal{T}_i} \mathbf{S}(\mathbf{W}^n) \, dV, \qquad (3)$$

where $N(i)$ is the set of neighboring triangles of the cell $\mathcal{T}_i$, $\mathbf{W}_i^n$ is an averaged value of the solution $\mathbf{W}$ in the cell $\mathcal{T}_i$ at time t_n,

$$\mathbf{W}_i = \frac{1}{|\mathcal{T}_i|} \int_{\mathcal{T}_i} \mathbf{W} \, dV,$$

where $|\mathcal{T}_i|$ denotes the area of $\mathcal{T}_i$. Here, Γ_{ij} is the interface between the two control volumes $\mathcal{T}_i$ and $\mathcal{T}_j$, $\mathbf{n} = (n_x, n_y)^T$ denotes the unit outward normal to Γ_{ij}, and $\mathcal{F}(\mathbf{W}; \mathbf{n})$ is the numerical flux defined as

$$\mathcal{F}(\mathbf{W}; \mathbf{n}) = \mathbf{F}(\mathbf{W}) n_x + \mathbf{G}(\mathbf{W}) n_y.$$

The finite volume discretization (3) is complete once the gradient fluxes $\mathcal{F}(\mathbf{W}; \mathbf{n})$ and a discretization of source terms $\mathbf{S}(\mathbf{W})$ are well defined.

4

3.1. *Discretization of the gradient fluxes*

Applied to the system (2), the finite volume discretization over the control volume $\mathcal{T}_i$ yields

$$\frac{\partial}{\partial t} \int_{\mathcal{T}_i} \phi h \, dV + \oint_{\mathcal{S}_i} (\phi h u n_x + \phi h v n_y) \, d\sigma = 0,$$

$$\frac{\partial}{\partial t} \int_{\mathcal{T}_i} \phi h u \, dV + \oint_{\mathcal{S}_i} \left(\left(\phi h u^2 + \frac{1}{2} g \phi h^2 \right) n_x + \phi h u v n_y \right) d\sigma =$$

$$\oint_{S_i} \phi \left(-g h Z n_x + \frac{1}{2} g h^2 n_x \right) d\sigma,$$

$$\tag{4}$$

$$\frac{\partial}{\partial t} \int_{\mathcal{T}_i} \phi h v \, dV + \oint_{\mathcal{S}_i} \left(\phi h u v n_x + \left(\phi h v^2 + \frac{1}{2} g \phi h^2 \right) n_y \right) d\sigma =$$

$$\oint_{S_i} \phi \left(-g h Z n_y + \frac{1}{2} g h^2 n_y \right) d\sigma,$$

where $\mathcal{S}_i$ is the surface surrounding the control volume $\mathcal{T}_i$. Note that the proposed finite volume discretization belongs to a class of Riemann problem solvers for which the water height h is constant in the control volume $\mathcal{T}_i$. Using the expressions of the normal velocity $u_\eta = u n_x + v n_y$ and tangential velocity $u_\tau = -u n_y + v n_x$, the above equations can be reformulated as

$$\frac{\partial}{\partial t} \int_{\mathcal{T}_i} \phi h \, dV + \oint_{\mathcal{S}_i} \phi h u_\eta \, d\sigma = 0,$$

$$\frac{\partial}{\partial t} \int_{\mathcal{T}_i} \phi h u \, dV + \oint_{\mathcal{S}_i} \left(\phi h u u_\eta + \frac{1}{2} g \phi h^2 n_x \right) d\sigma =$$

$$- \oint_{S_i} g \phi h Z n_x \, d\sigma + \oint_{S_i} \frac{1}{2} g \phi h^2 n_x \, d\sigma,$$

$$\tag{5}$$

$$\frac{\partial}{\partial t} \int_{\mathcal{T}_i} \phi h v \, dV + \oint_{\mathcal{S}_i} \left(\phi h v u_\eta + \frac{1}{2} g \phi h^2 n_y \right) d\sigma =$$

$$- \oint_{S_i} g \phi h Z n_y \, d\sigma + \oint_{S_i} \frac{1}{2} g \phi h^2 n_y \, d\sigma,$$

In order to simplify the system (5), we first sum the second equation multiplied by n_x to the third equation multiplied by n_y, then we subtract the third equation multiplied by n_x from the second equation multiplied by n_y. The result of these

operations is

$$\frac{\partial}{\partial t} \int_{\mathcal{T}_i} \phi h \, dV + \oint_{\mathcal{S}_i} \phi h u_\eta \, d\sigma = 0,$$

$$\frac{\partial}{\partial t} \int_{\mathcal{T}_i} \phi h u_\eta \, dV + \oint_{\mathcal{S}_i} \left(\phi h u_\eta u_\eta + \frac{1}{2} g \phi h^2 \right) d\sigma = - \oint_{S_i} g \phi h Z \, d\sigma + \oint_{S_i} \frac{1}{2} g \phi h^2 \, d\sigma,$$

$$(6)$$

$$\frac{\partial}{\partial t} \int_{\mathcal{T}_i} \phi h u_\tau \, dV + \oint_{\mathcal{S}_i} \phi h u_\tau u_\eta \, d\sigma = 0,$$

which can be reformulated in a differential form as

$$\frac{\partial \phi h}{\partial t} + \frac{\partial \left(\phi h u_\eta \right)}{\partial \eta} = 0,$$

$$\frac{\partial \left(\phi h u_\eta \right)}{\partial t} + \frac{\partial}{\partial \eta} \left(\phi h u_\eta^2 + \frac{1}{2} g \phi h^2 \right) = -g \phi h \frac{\partial Z}{\partial \eta} + \frac{1}{2} g h^2 \frac{\partial \phi}{\partial \eta},$$

$$\frac{\partial \left(\phi h u_\tau \right)}{\partial t} + \frac{\partial}{\partial \eta} \left(\phi h u_\eta u_\tau \right) = 0, \qquad (7)$$

$$\frac{\partial Z}{\partial t} = 0,$$

$$\frac{\partial \phi}{\partial t} = 0.$$

Notice that the last two equations in (7) have been included in the system to formulate the projected system in a advective form without source terms. Thus, an equivalent system of (7) can also be rewritten in a vector form as

$$\frac{\partial \mathbf{U}}{\partial t} + \mathbf{A}_\eta(\mathbf{U}) \frac{\partial \mathbf{U}}{\partial \eta} = \mathbf{0}. \qquad (8)$$

where

$$\mathbf{U} = \begin{pmatrix} \phi h \\ \phi h u_\eta \\ \phi h u_\tau \\ Z \\ \phi \end{pmatrix}, \qquad \mathbf{A}_\eta(\mathbf{U}) = \begin{pmatrix} 0 & 1 & 0 & 0 & 0 \\ gh - u_\eta^2 & 2u_\eta & 0 & \phi gh & -gh^2 \\ -u_\eta u_\tau & u_\tau & u_\eta & 0 & 0 \\ 0 & 0 & 0 & 0 & 0 \\ 0 & 0 & 0 & 0 & 0 \end{pmatrix}.$$

One of the advantages in considering the projected system (8) is that no discretization of source terms is required. Thus, in the predictor stage, we use the projected system (8) to compute the averaged states as

$$\mathbf{U}_{ij}^n = \frac{1}{2} \left(\mathbf{U}_i^n + \mathbf{U}_j^n \right) - \frac{1}{2} \operatorname{sgn} \left[\mathbf{A}_\eta \left(\overline{\mathbf{U}} \right) \right] \left(\mathbf{U}_j^n - \mathbf{U}_i^n \right), \qquad (9)$$

where the sign matrix of the Jacobian is defined as

$$\text{sgn}\left[\nabla \mathbf{F}_\eta\left(\overline{\mathbf{U}}\right)\right] = \mathcal{R}(\overline{\mathbf{U}})\,\text{sgn}\left[\Lambda(\overline{\mathbf{U}})\right]\mathcal{R}^{-1}(\overline{\mathbf{U}}),$$

with $\Lambda(\overline{\mathbf{U}})$ is the diagonal matrix of eigenvalues, and $\mathcal{R}(\overline{\mathbf{U}})$ is the right eigenvector matrix. These matrices can be explicitly expressed using the associated eigenvalues of $\mathbf{A}_\eta(\mathbf{U})$ in (8). Here, $\overline{\mathbf{U}}$ is the Roe's averaged state given by

$$\overline{\mathbf{U}} = \begin{pmatrix} \dfrac{h_i + h_j}{2}\dfrac{\phi_i + \phi_j}{2} \\[2ex] \dfrac{h_i + h_j}{2}\left(\dfrac{u_i\sqrt{h_i} + u_j\sqrt{h_j}}{\sqrt{h_i} + \sqrt{h_j}}n_x + \dfrac{v_i\sqrt{h_i} + v_j\sqrt{h_j}}{\sqrt{h_i} + \sqrt{h_j}}n_y\right)\dfrac{\phi_i + \phi_j}{2} \\[3ex] \dfrac{h_i + h_j}{2}\left(-\dfrac{u_i\sqrt{h_i} + u_j\sqrt{h_j}}{\sqrt{h_i} + \sqrt{h_j}}n_y + \dfrac{v_i\sqrt{h_i} + v_j\sqrt{h_j}}{\sqrt{h_i} + \sqrt{h_j}}n_x\right)\dfrac{\phi_i + \phi_j}{2} \\[3ex] \dfrac{Z_i + Z_j}{2} \\[2ex] \dfrac{\phi_i + \phi_j}{2} \end{pmatrix}. \qquad (10)$$

Once the states $\mathbf{U}_{ij}^n$ are calculated in the predictor stage (9), the states $\mathbf{W}_{ij}^n$ are recovered by using the transformations $v = (u_\tau, u_\eta) \cdot \eta$ and $u = (u_\tau, u_\eta) \cdot \tau$. Thus, applied to the system (2), the proposed finite volume method consists of a predictor stage and a corrector stage and can be formulated as

$$\mathbf{U}_{ij}^n = \frac{1}{2}\left(\mathbf{U}_i^n + \mathbf{U}_j^n\right) - \frac{1}{2}\,\text{sgn}\left[\mathbf{A}_\eta\left(\overline{\mathbf{U}}\right)\right]\left(\mathbf{U}_j^n - \mathbf{U}_i^n\right),$$

$$(11)$$

$$\mathbf{W}_i^{n+1} = \mathbf{W}_i^n - \frac{\Delta t}{|\mathcal{T}_i|}\sum_{j \in N(i)}\mathcal{F}\left(\mathbf{W}_{ij}^n; \eta_{ij}\right)|\Gamma_{ij}| + \Delta t\mathbf{S}_i^n,$$

Next we discuss the formulation of matrices $\mathcal{R}(\overline{\mathbf{U}})$ and $\mathcal{R}^{-1}(\overline{\mathbf{U}})$, the treatment of source terms $\mathbf{S}_i^n$ in the proposed finite volume scheme and also the extension of the scheme to a second-order accuracy.

3.2. *Determination of the sign matrix*

The eigenvalues corresponding to the projected system (8) are

$$\overline{\lambda}_1 = \overline{u}_\eta - \sqrt{g\overline{h}},$$

$$\overline{\lambda}_2 = \overline{u}_\eta + \sqrt{g\overline{h}},$$

$$\overline{\lambda}_3 = \overline{u}_\eta,$$

$$\overline{\lambda}_4 = 0,$$

$$\overline{\lambda}_5 = 0.$$

Hence, the sign matrix in (9) is defined as

$$\text{sgn}\Big[\mathbf{A}_\eta\left(\overline{\mathbf{U}}\right)\Big] = \mathcal{R}(\overline{\mathbf{U}})\,\text{sgn}\Big[\Lambda(\overline{\mathbf{U}})\Big]\mathcal{R}^{-1}(\overline{\mathbf{U}}),$$

where $\overline{\mathbf{U}}$ is the Roe's average state given by (10), $\mathcal{R}(\overline{\mathbf{U}})$ and $\Lambda(\overline{\mathbf{U}})$ are respectively, the right eigenvector and the diagonal matrices reconstructed as

$$\mathcal{R}(\overline{\mathbf{U}}) = \begin{pmatrix} 1 & 1 & 0 & 0 & 1 \\ \bar{u}_\eta - \bar{c} & \bar{u}_\eta + \bar{c} & 0 & 0 & 0 \\ \bar{u}_\tau & \bar{u}_\tau & 1 & 0 & \bar{u}_\tau \\ 0 & 0 & 0 & 1 & 0 \\ 0 & 0 & 0 & \dfrac{\overline{\phi}}{\bar{h}} & \dfrac{\bar{c}^2 - \bar{u}_\eta^2}{g\bar{h}^2} \end{pmatrix}, \qquad \Lambda(\overline{\mathbf{U}}) = \begin{pmatrix} \bar{\lambda}_1 & 0 & 0 & 0 & 0 \\ 0 & \bar{\lambda}_2 & 0 & 0 & 0 \\ 0 & 0 & \bar{\lambda}_3 & 0 & 0 \\ 0 & 0 & 0 & \bar{\lambda}_4 & 0 \\ 0 & 0 & 0 & 0 & \bar{\lambda}_5 \end{pmatrix},$$

and

$$\mathcal{R}^{-1}(\overline{\mathbf{U}}) = \begin{pmatrix} \dfrac{\bar{u}_\eta + \bar{c}}{2\bar{c}} & \dfrac{-1}{2\bar{c}} & 0 & \dfrac{-\overline{\phi}\bar{c}}{2(\bar{u}_\eta - \bar{c})} & \dfrac{\bar{h}\bar{c}}{2(\bar{u}_\eta - \bar{c})} \\ \dfrac{-\bar{u}_\eta - \bar{c}}{2\bar{c}} & \dfrac{1}{2\bar{c}} & 0 & \dfrac{\overline{\phi}\bar{c}}{2(\bar{u}_\eta + \bar{c})} & \dfrac{-\bar{h}\bar{c}}{2(\bar{u}_\eta + \bar{c})} \\ -\bar{u}_\tau & 0 & 1 & 0 & 0 \\ 0 & 0 & 0 & 1 & 0 \\ 0 & 0 & 0 & \dfrac{-\overline{\phi}\bar{c}^2}{\bar{c}^2 - \bar{u}_\eta^2} & \dfrac{\overline{\phi}\bar{c}^2}{\bar{c}^2 - \bar{u}_\eta^2} \end{pmatrix},$$

where $\bar{c} = \sqrt{g\bar{h}}$. Once the matrices $\mathcal{R}(\overline{\mathbf{U}})$ and $\mathcal{R}^{-1}(\overline{\mathbf{U}})$ are calculated the sign matrix can be easily updated according to (9).

3.3. *Discretization of the source term*

The treatment of the source terms in the shallow water equations presents a challenge in many numerical methods, compare [3, 21] among others. In our scheme, the source term approximation $\mathbf{S}_i^n$ in the corrector stage is reconstructed such that the still-water equilibrium (C-property) [6] is satisfied. Here, a numerical scheme is said to satisfy the C-property for the equations (2) if the condition

$$u = v = 0, \qquad h + Z = C, \tag{12}$$

holds for stationary flows at rest. In (12), C is nonnegative constant. Therefore, the treatment of source terms in (11) is reconstructed such that the condition (12) is preserved at the discretized level. Hence, $\mathbf{S}_i^n$ should be a consistent discretization
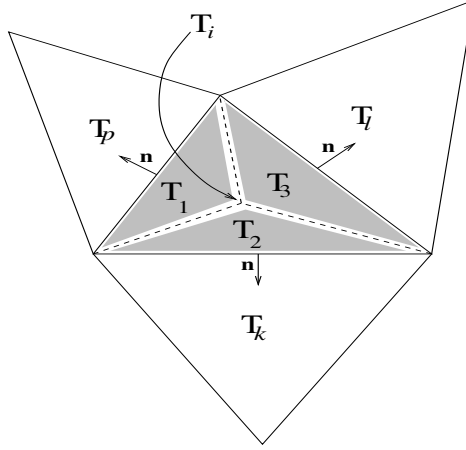
Figure 2. Sub-triangles used in the discretization of source terms.

of the source term in (2) defined as

$$
\mathbf{S}_i^n = \begin{pmatrix} 0 \\ -g\bar{h}_{xi}^n\bar{\phi}_{xi}^n \displaystyle\sum_{j \in N(i)} Z_{ij}n_{xij}\,|\Gamma_{ij}| \\ -g\bar{h}_{yi}^n\bar{\phi}_{yi}^n \displaystyle\sum_{j \in N(i)} Z_{ij}n_{yij}\,|\Gamma_{ij}| \\ 0 \end{pmatrix}.
\tag{13}
$$

The approximations $\bar{h}_{xi}^n$ and $\bar{h}_{yi}^n$ are reconstructed using a technique recently developed in [3] for the proposed finite volume method to satisfy the well-known C-property in the standard shallow water flow over fixed beds. In this section we briefly describe the formulation of this procedure and more details can be found in [3]. Hence, at the stationary state, the numerical flux in the corrector stage yields

$$
\sum_{j \in N(i)} \mathcal{F}\left(\mathbf{W}_{ij}^n; \mathbf{n}_{ij}\right) = \begin{pmatrix} 0 \\ -g \displaystyle\int_{\mathcal{T}_i} \phi h \frac{\partial Z}{\partial x} + \frac{1}{2}g \int_{\mathcal{T}_i} h^2 \frac{\partial \phi}{\partial x}\, dV \\ -g \displaystyle\int_{\mathcal{T}_i} \phi h \frac{\partial Z}{\partial y} + \frac{1}{2}g \int_{\mathcal{T}_i} h^2 \frac{\partial \phi}{\partial y}\, dV \\ 0 \\ 0 \end{pmatrix},
$$

which is equivalent to

9

$$
\begin{pmatrix}
0 \\
\displaystyle\sum_{j\in N(i)} \frac{1}{2}g((\phi h)_{ij}^n)^2 N_{xij} \\
\displaystyle\sum_{j\in N(i)} \frac{1}{2}g((\phi h)_{ij}^n)^2 N_{yij} \\
0 \\
0
\end{pmatrix}
=
\begin{pmatrix}
0 \\
-g\displaystyle\int_{\mathcal{T}_i} \phi h\frac{\partial Z}{\partial x} + \frac{1}{2}g\displaystyle\int_{\mathcal{T}_i} h^2\frac{\partial \phi}{\partial x}\,dV \\
-g\displaystyle\int_{\mathcal{T}_i} \phi h\frac{\partial Z}{\partial y} + \frac{1}{2}g\displaystyle\int_{\mathcal{T}_i} h^2\frac{\partial \phi}{\partial y}\,dV \\
0 \\
0
\end{pmatrix}.
\qquad (14)
$$

where $N_{xij} = n_{xij}\,|\Gamma_{ij}|$ and $N_{yij} = n_{yij}\,|\Gamma_{ij}|$. Next, to approximate the source terms we proceed as follows. First we decompose the triangle $\mathcal{T}_i$ into three sub-triangles as depicted in Figure 2. Then, the source term is approximated as

$$
\int_{\mathcal{T}_i} \phi h\frac{\partial Z}{\partial x}\,dV \approx \phi_i \int_{\mathcal{T}_i} h\frac{\partial Z}{\partial x}\,dV
$$

$$
= \phi_i \left(\int_{\mathcal{T}_1} h\frac{\partial Z}{\partial x}\,dV + \int_{\mathcal{T}_2} h\frac{\partial Z}{\partial x}\,dV + \int_{\mathcal{T}_3} h\frac{\partial Z}{\partial x}\,dV \right), \qquad (15)
$$

where

$$
\int_{\mathcal{T}_1} h\frac{\partial Z}{\partial x}\,dV \approx h_1 \int_{\mathcal{T}_1} \frac{\partial Z}{\partial x}\,dV,
$$

with h_1 is an average value of h on the sub-triangle $\mathcal{T}_1$. Hence,

$$
\int_{T_1} h\frac{\partial Z}{\partial x}\,dV \approx h_1 \sum_{j\in N(1)} \int_{\Gamma_{1j}} Z n_x\,d\sigma,
$$

$$
= h_1 \sum_{j\in N(1)} Z_{1j} N_{x_{1j}},
$$

$$
= h_1 \sum_{j\in N(1)} \frac{Z_1 + Z_j}{2} N_{x_{1j}}. \qquad (16)
$$

Again, using the stationary flow condition $h_1 + Z_1 = C$ and $h_j + Z_j = C$, one gets

$$
h_1 + Z_1 + h_j + Z_j = 2C \qquad \text{and} \qquad \frac{Z_1 + Z_j}{2} = C - \frac{h_1 + h_j}{2}.
$$

Thus, (16) gives

$$
\int_{\mathcal{T}_1} h\frac{\partial Z}{\partial x}\,dV = h_1 \sum_{j\in N(1)} \left(C - \frac{h_1 + h_j}{2} \right) N_{x1j}.
$$

Using the fact that $\sum_{j \in N(1)} N_{x1j} = 0$,

$$\int_{\mathcal{T}_1} h \frac{\partial Z}{\partial x}\, dV = -\frac{h_1}{2} \sum_{j \in N(1)} h_j\, N_{x1j},$$

$$= -\frac{h_1}{2}\Big(h_p N_{x1p} + h_2 N_{x12} + h_3 N_{x13}\Big).$$

A similar procedure leads to the following approximations of the other terms in (15)

$$\int_{\mathcal{T}_2} h \frac{\partial Z}{\partial x}\, dV = -\frac{h_2}{2}\Big(h_k N_{x2k} + h_1 N_{x21} + h_3 N_{x23}\Big),$$

$$\int_{\mathcal{T}_3} h \frac{\partial Z}{\partial x}\, dV = -\frac{h_3}{2}\Big(h_l N_{x3l} + h_1 N_{x31} + h_2 N_{x32}\Big).$$

Notice that h_p, h_k and h_l are the averaged values of h respectively, on the triangle $\mathcal{T}_p$, $\mathcal{T}_k$ and $\mathcal{T}_l$, see Figure 2. Summing up, the discretization (15) gives

$$\int_{\mathcal{T}_i} \phi h \frac{\partial Z}{\partial x}\, dV = -\frac{\phi_i h_1}{2} h_p N_{x1p} - \frac{\phi_i h_2}{2} h_k N_{x2k} - \frac{\phi_i h_3}{2} h_l N_{x3l}.$$

For this reconstruction, the source terms in (14) result in

$$\sum_{j \in N(i)} \Big((\phi h)_{ij}^n\Big)^2 N_{xij} = \phi_i\Big(h_1\left(h_p N_{x1p}\right) + h_2\left(h_k N_{x2k}\right) + h_3\left(h_l N_{x3l}\right)\Big)+,$$

$$\frac{1}{2}\Big(h_1^2(\phi_p - \phi_i)N_{x1p} + h_2^2(\phi_k - \phi_i)N_{x2k} + h_3^2(\phi_l - \phi_i)N_{x3l}\Big),$$

$$\tag{17}$$

$$\sum_{j \in N(i)} \Big((\phi h)_{ij}^n\Big)^2 N_{yij} = \phi_i\Big(h_1\Big(h_p N_{y1p}\Big) + h_2\Big(h_k N_{y2k}\Big) + h_3\left(h_l N_{y3l}\right)\Big) +$$

$$\frac{1}{2}\Big(h_1^2(\phi_p - \phi_i)N_{y1p} + h_2^2(\phi_k - \phi_i)N_{y2k} + h_3^2(\phi_l - \phi_i)N_{y3l}\Big).$$

Here, (17) forms a nonlinear system of two equations for the three unknowns h_1, h_2 and h_3. To complete the system we add the natural conservation equation

$$h_1 + h_2 + h_3 = 3h_i.$$

To solve the nonlinear system we use a Newton-Raphson type algorithm. Analogously, the bottom values Z_j, $j = 1, 2, 3$ are reconstructed in each sub-triangle of $\mathcal{T}_i$ as

$$Z_j + h_j^n = Z_i + h_i^n, \qquad j = 1, 2, 3.$$

Finally, the source terms in (15) are approximated as

$$\phi_i h_1 \int_{\mathcal{T}_1} \frac{\partial Z}{\partial x} \, dV = \phi_i h_1 \left(\frac{Z_1 + Z_p}{2} N_{x1p} + \frac{Z_1 + Z_2}{2} N_{x12} + \frac{Z_1 + Z_3}{2} N_{x13} \right),$$

$$\phi_i h_2 \int_{\mathcal{T}_1} \frac{\partial Z}{\partial x} \, dV = \phi_i h_2 \left(\frac{Z_2 + Z_k}{2} N_{x2k} + \frac{Z_2 + Z_1}{2} N_{x21} + \frac{Z_2 + Z_3}{2} N_{x23} \right), \quad (18)$$

$$\phi_i h_3 \int_{\mathcal{T}_1} \frac{\partial Z}{\partial x} \, dV = \phi_i h_3 \left(\frac{Z_3 + Z_l}{2} N_{x3l} + \frac{Z_3 + Z_1}{2} N_{x31} + \frac{Z_3 + Z_2}{2} N_{x32} \right),$$

and

$$\int_{\mathcal{T}_1} h^2 \frac{\partial \phi}{\partial x} \, dV = \frac{h_1^2}{2} \left(\phi_p N_{x1p} + \phi_i N_{x12} + \phi_i N_{x13} \right),$$

$$\int_{\mathcal{T}_2} h^2 \frac{\partial \phi}{\partial x} \, dV = \frac{h_2^2}{2} \left(\phi_k N_{x2k} + \phi_i N_{x21} + \phi_i N_{x23} \right), \quad (19)$$

$$\int_{\mathcal{T}_3} h^2 \frac{\partial \phi}{\partial x} \, dV = \frac{h_3^2}{2} \left(\phi_l N_{x3l} + \phi_i N_{x31} + \phi_i N_{x32} \right),$$

with a similar equation for the other source terms in the y-direction. Numerical results reported in [3] for shallow water flows with constant porosity have shown that the above reconstruction exactly preserves the C-property to the machine precision.

3.4. *Second-order reconstruction*

It is clear that the discretization (11) is only first-order accurate. In order to develop a second-order finite volume scheme, we use a MUSCL method incorporating slope limiters in the spatial approximation and a two-step Runge-Kutta method for time integration. The MUSCL discretization uses an approximation of the solution state $\mathbf{W}$ by linear interpolation at each cell interface Γ_{ij} involving combinations of upwind and centered gradients as

$$\mathbf{W}_{ij} = \mathbf{W}_i + \frac{1}{2} \left(\beta \nabla \mathbf{W}_i \cdot \overrightarrow{\mathbf{X}_i \mathbf{X}_j} + (1 - \beta)(\mathbf{W}_j - \mathbf{W}_i) \right),$$

$$\mathbf{W}_{ji} = \mathbf{W}_j - \frac{1}{2} \left(\beta \nabla \mathbf{W}_j \cdot \overrightarrow{\mathbf{X}_i \mathbf{X}_j} + (1 - \beta)(\mathbf{W}_j - \mathbf{W}_i) \right), \quad (20)$$

where $\mathbf{X}_i = (x_i, y_i)^T$ and $\mathbf{X}_j = (x_j, y_j)^T$ are the barycentre coordinates of cells $\mathcal{T}_i$ and $\mathcal{T}_j$, respectively. Thus, the cell gradients are evaluated by minimizing the quadratic functional

$$\Psi_i(X, Y) = \sum_{j \in m(i)} \left| \mathbf{W}_i + (x_j - x_i)X + (y_j - y_i)Y - \mathbf{W}_j \right|^2, \quad (21)$$

where $m(i)$ is the set of indices of neighboring cells that have a common edge or vertex with the control volume $\mathcal{T}_i$. Thus, the cell gradients $\nabla \mathbf{W}_i = \left(\frac{\partial \mathbf{W}_i}{\partial x}, \frac{\partial \mathbf{W}_i}{\partial y} \right)^T$

in (20) are solutions of the linear system

$$\frac{\partial \Psi_i}{\partial X}(X, Y) = 0, \qquad \frac{\partial \Psi_i}{\partial Y}(X, Y) = 0.$$

It is easy to verify that

$$\frac{\partial \mathbf{W}_i}{\partial x} = \frac{I_{yy}}{D_{xy}}\mathbf{J}_x - \frac{I_{xy}}{D_{xy}}\mathbf{J}_y, \qquad \frac{\partial \mathbf{W}_i}{\partial y} = \frac{I_{xx}}{D_{xy}}\mathbf{J}_y - \frac{I_{yx}}{D_{xy}}\mathbf{J}_x, \tag{22}$$

where $D_{xy} = I_{xx}I_{yy} - I_{xy}I_{yx}$,

$$I_{xx} = \sum_{j \in m(i)} (x_j - x_i)^2, \qquad I_{yy} = \sum_{j \in m(i)} (y_j - y_i)^2,$$

$$I_{xy} = I_{yx} = \sum_{j \in m(i)} (x_j - x_i)(y_j - y_i),$$

$$\mathbf{J}_x = \sum_{j \in m(i)} (x_j - x_i)(\mathbf{W}_j - \mathbf{W}_i), \qquad \mathbf{J}_y = \sum_{j \in m(i)} (y_j - y_i)(\mathbf{W}_j - \mathbf{W}_i).$$

In (20), β represents a parameter between 0 and 1. This parameter contains the amount of upwinding at each cell and is taken in practice as $\beta = \dfrac{2}{3}$. The resulting scheme is second-order accurate in space but is not necessarily monotone and non-physical oscillations are produced. To damp the numerical oscillation, we incorporate slope limiters to the reconstruction (20) as

$$\mathbf{W}_{ij} = \mathbf{W}_i + \frac{1}{2}\lim\left(\beta \nabla \mathbf{W}_i \cdot \overrightarrow{\mathbf{X}_i\mathbf{X}_j} + (1-\beta)(\mathbf{W}_j - \mathbf{W}_i), \mathbf{W}_j - \mathbf{W}_i\right),$$

$$\mathbf{W}_{ji} = \mathbf{W}_j - \frac{1}{2}\lim\left(\beta \nabla \mathbf{W}_j \cdot \overrightarrow{\mathbf{X}_i\mathbf{X}_j} + (1-\beta)(\mathbf{W}_j - \mathbf{W}_i), \mathbf{W}_j - \mathbf{W}_i\right), \tag{23}$$

As example of slope limiter functions, we consider the MinMod limiter function given by

$$\lim(a, b) = \begin{cases} \text{sgn}(a)\, \min\left(|a|, |b|\right), & \text{if } ab > 0, \\[2mm] 0, & \text{otherwise.} \end{cases} \tag{24}$$

It should be pointed out that other slope limiter functions from [16] can also be implemented in our finite volume method without major conceptual modifications. In addition, the treatment of boundary conditions in the proposed finite volume method is performed using similar techniques as those described in [2]. For the computational examples considered in this paper, boundary conditions are enforced on the corrector solution by computing fluxes at boundaries. On the predictor solution and the slopes of dependent variables, boundary conditions are enforced in boundary cells by setting the required variables to the corresponding values of

the adjacent inner cells. When slopes are based on vertex values, the solution at boundary vertices is computed by interpolation from two neighboring centroids. When slopes are based on centroid values, the three points used to estimate the slopes are the centroid and the two neighboring centroids inside the computational domain. For further details on the implementation of boundary conditions for the proposed non-homogeneous Riemann solver we refer to [2, 18].

4. Numerical Results

We present numerical results for a class of test problems for dam-break flows over porous beds. In all the computations reported herein, the gravitational acceleration is fixed to $g = 9.81 \ m/s^2$, the Courant number Cr is set to 0.8 and the time stepsize Δt is adjusted at each step according to the stability condition

$$\Delta t = Cr \min_{\Gamma_{ij}} \left(\frac{|\mathcal{T}_i| + |\mathcal{T}_j|}{2 \, |\Gamma_{ij}| \max_p |(\lambda^p)_{ij}|} \right),$$

where Γ_{ij} is the edge between two cells $\mathcal{T}_i$ and $\mathcal{T}_j$. It should be pointed out that the treatment of boundary conditions in our finite volume method is performed using similar techniques as those described in [2]. For the computational examples considered in this paper, boundary conditions are enforced on the corrector solution by computing fluxes at boundaries. On the predictor solution and the slopes of dependent variables, boundary conditions are enforced in boundary cells by setting the required variables to the corresponding values of the adjacent inner cells. When slopes are based on vertex values, the solution at boundary vertices is computed by interpolation from two neighboring centroids. When slopes are based on centroid values, the three points used to estimate the slopes are the centroid and the two neighboring centroids inside the computational domain. For further details on the implementation of boundary conditions for finite volume methods we refer to [2, 5] among others.

4.1. *Verification of the C-property*

First we consider the problem of water flow in two-dimensional channel including three humps to verify the C-property in our method. The mathematical formulation consists on solving the equations (1) in a computational domain $[0, 10] \times [0, 5]$ subject to the following initial conditions

$$h(0, x, y) = 1 - Z(x, y), \qquad u(0, x, y) = v(0, x, y) = 0 \ m/s,$$

where the hump is defined by

$$Z(x, y) = 0.2 \exp\left(-4(x-4)^2 - 4(y-2.5)^2\right) + 0.4 \exp\left(-4(x-6)^2 - 4(y-1.5)^2\right)$$
$$+ 0.4 \exp\left(-4(x-6)^2 - 4(y-3.5)^2\right).$$

The porosity is assumed to be variable within the bed and it is defined as
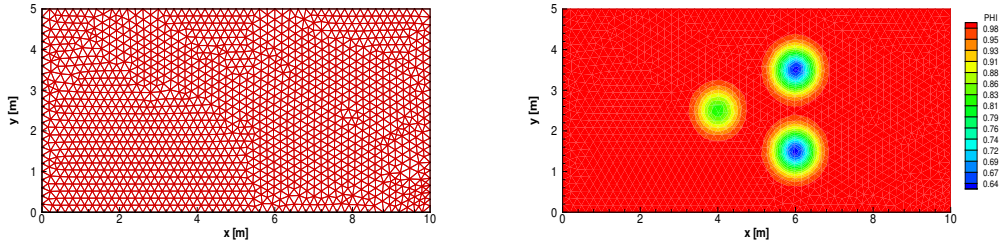
$$\Phi(x, y) = 1 - Z(x, y).$$

14

Figure 3. Mesh (left) and porosity (right) for the test example used for verification of the C-property.
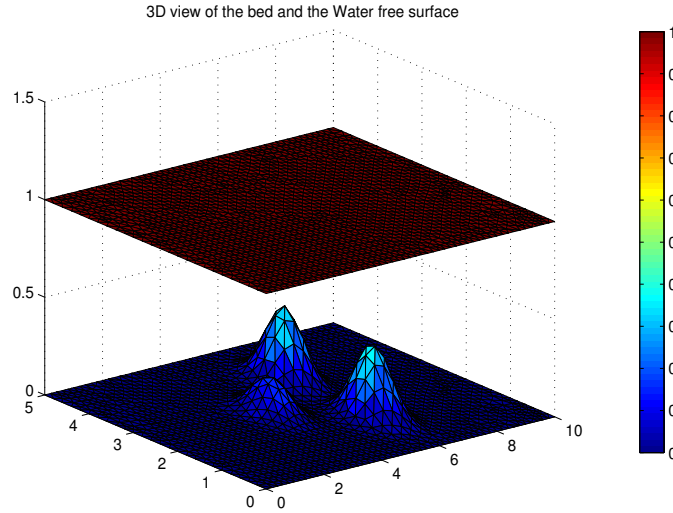

Figure 4. Water free-surface for the test example used for verification of the C-property.

In Figure 6 we present the plot of the porosity along with the unstructured mesh used in our simulations. Here the mesh contains 2795 triangles and 1474 nodes. It is clear that the porosity varies within the bed and it vanishes wherever the bed is flat.

The purpose of this test example is to verify the achievement of the C-property for the considered finite volume method applied to porous shallow water flows over non-flat bottom. In Figure 4 we present the water free-surface obtained at time $t = 90$ s. As expected the water free-surface remains constant during the simulation times and the proposed non-homogeneous Riemann solver preserves the C-property. In order to quantify the results for this test example we summarize in Table 1 the L^1 errors in the water velocity u, water velocity v and the water free-surface $h + Z$ at times $t = 30$ s, 60 s and 90 s. It is clear that our method gives roughly the same errors for all considered water solutions. The differences of the numerical solution from the exact solution, in terms of water free-surface, are due to round-off errors. The non-homogeneous Riemann solver preserves the C-property for this two-dimensional test example.

Next we consider the same test example but with a more complex porosity function than the previous simulations. For this case the porosity does not follow the bed trend and it is depicted in Figure 5. The computed L^1 errors are summarized in Table 2 for the water velocity u, water velocity v and the water free-surface $h + Z$ at times $t = 30$ s, 60 s and 90 s. As can be seen from the obtained results, the proposed method exactly preserves the well-balanced property at the machine precision for this test example.

15

Table 1. L^1-error norms of the water velocity u, water velocity v and the water free-surface for the test example used for verification of the C-property at times $t = 30\ s$, $60\ s$ and $90\ s$.

t	Error in u	Error in v	Error in $h + Z$
$30\ s$	2.65E-14	1.08E-14	4.47E-16
$60\ s$	3.82E-14	2.56E-14	7.25E-16
$90\ s$	5.20E-14	3.38E-14	8.15E-16
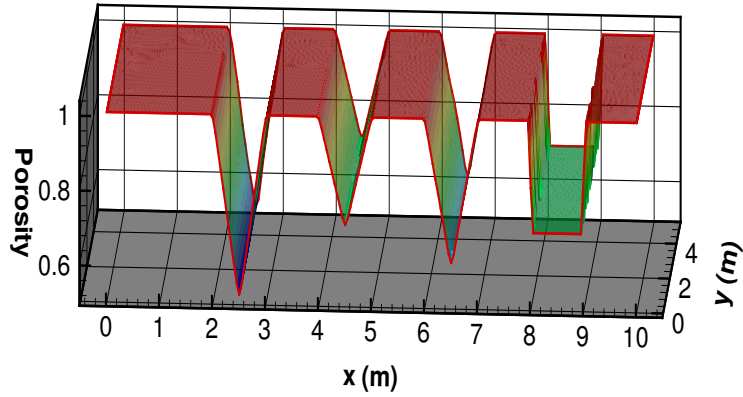
Figure 5. Porosity function for the test example used for verification of the C-property.

Table 2. L^1-error norms of the water velocity u, water velocity v and the water free-surface for the test example with complex porosity used for verification of the C-property at times $t = 30\ s$, $60\ s$ and $90\ s$.

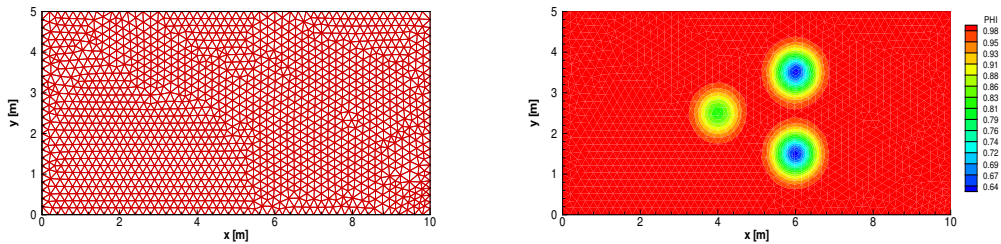| t	Error in u	Error in v	Error in $h + Z$
$30\ s$	2.83E-14	1.20E-14	4.62E-16
$60\ s$	3.95E-14	2.67E-14	7.49E-16
$90\ s$	5.41E-14	3.58E-14	8.38E-16

Figure 6. Mesh (left) and porosity (right) for the test example used for verification of the C-property.
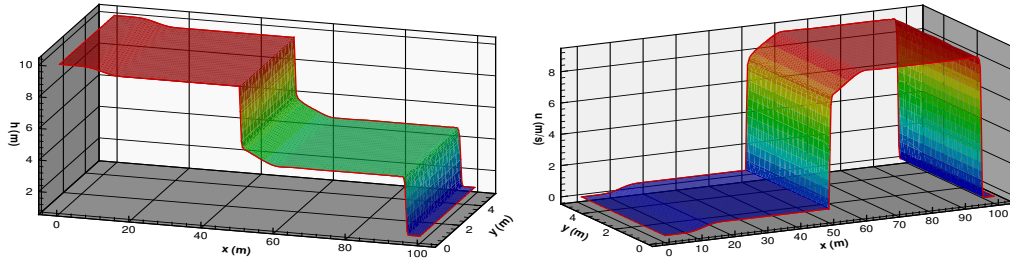
Figure 7. Water height h (left) and water velocity u (right) for the test example of dam-break problem with variable porosity at time $t = 4\ s$.
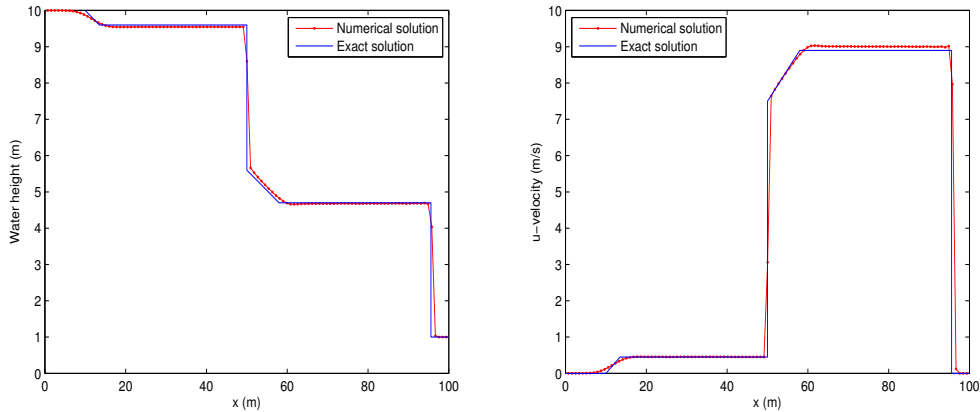

Figure 8. Cross-section of water height h (left) and of water velocity u (right) for the test example of dam-break problem with variable porosity at time $t = 4\ s$.

4.2. *Dam-break problem with variable porosity*

Our second test example consists of dam-break problem with a porosity discontinuity proposed in [11]. In this test the porosity is equal to unity on the upstream side of the dam and is smaller ($\Phi = 0.1$) on the downstream side of the dam. Here we solve the equations (1) in a flat rectangular domain $[0, 100\ m] \times [0, 5\ m]$ with a dam located at $x_0 = 50\ m$. Initially,

$$h(0, x, y) = \begin{cases} 10\ m, & \text{if} \quad x \leq x_0, \\ 1\ m, & \text{elsewhere,} \end{cases} \qquad u(0, x, y) = v(0, x, y) = 0\ m/s.$$

We run the simulation using an unstructured mesh containing 4382 elements and 2404 nodes. Figure 7 illustrates the computed water height h and water velocity u at time $t = 4\ s$. As can be observed from these results, the dam-break flow with variable porosity can build up a heavily concentrated wavefront, which is bounded by the wave forefront and a contact discontinuity of the water free-surface, and depresses in the long run. The porosity variation can strongly modify the water free-surface profiles, and may have considerable implications for flood predictions. The proposed finite volume method accurately captures the shock and rarefaction waves in this dam-break problem. Note that the performance of the non-homogeneous Riemann solver is very attractive since the computed solutions remain stable and accurate even when coarse meshes are used without requiring complicated techniques to balance the source terms and flux gradients as those reported in [7] among others.
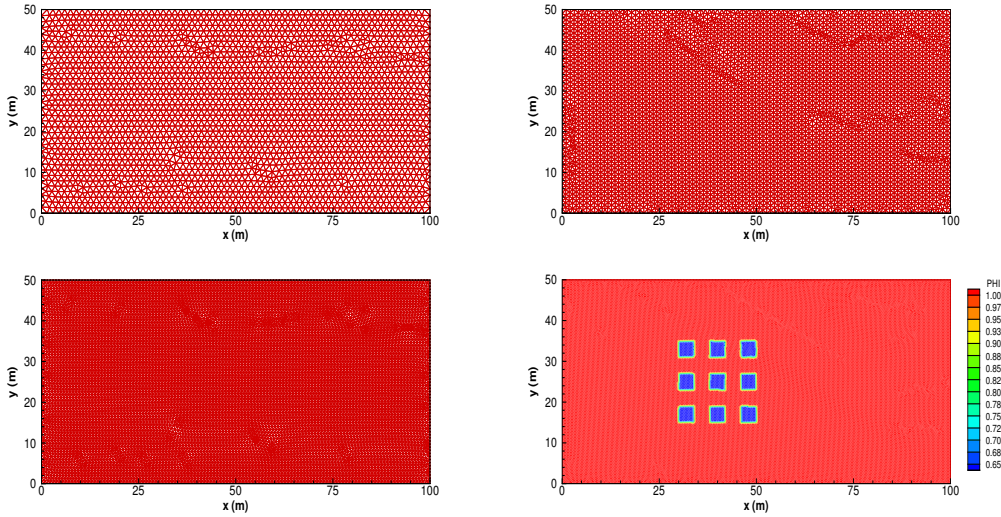
17

Figure 9. Mesh (left) and porosity (right) for the test example of shallow water flows over porous bed.

In Figure 8 we plot the water height h and the water velocity velocity u in x-direction along with the analytical solutions from [11]. There is an excellent agreement between the numerical results obtained by our finite volume method and the analytical solutions. The non-homogeneous Riemann solver performs well for this unsteady test example and reproduces the solutions without requiring fine meshes.

4.3. *Shallow water flows over porous bed*

We now consider the problem of dam-break over nine squared obstacles studied for example in [7, 11]. We consider a channel 100 m long and 50 m wide with a bed slope of 0.1% in the longitudinal direction and nine squared obstacles located in the channel region $[30, 50] \times [15, 35]$. The porosity of this region is defined as $\Phi = 1 - S/400$, with S being the horizontal area of all the obstacles expressed in square meters. In the rest of the domain the porosity is one, compare the plot of porosity in Figure 9. A total water discharge of 50 m^3/s is imposed at the inlet boundary, and the water depth is fixed to 1 m at the outlet boundary. The purpose of this test example is to examine the performance of the proposed method to resolve the moving fronts over complex topography. Figure 9 shows the three meshes used in our simulations for which the number of elements is 5044, 10322 and 20176 for Mesh A, Mesh B and Mesh C, respectively. The number of nodes for Mesh A, Mesh B and Mesh C is 2623, 5305 and 10289, respectively.

In Figure 10 we display cross-section of water height h at $y = 30$ m and $y = 45$ m at time $t = 90$ s using the three considered meshes. It is evident that results obtained using the Mesh C are more accurate than those obtained using Mesh B and Mesh A. However, the differences between these results are very small which confirms the grid convergence in the proposed finite volume method. Figure 11 depicts snapshots of the water height h and water velocity u at times $t = 60$ s, 90 s and 120 s using the Mesh B. As can be observed from these results, the propagation of the flood over obstacle region has been accurately captured by our finite volume method. During the flood propagation, the water free-surface creates a strong interaction with the nine obstacles, resulting in the formation of strong and weak shocks. By using the non-homogeneous Riemann solver, high resolution
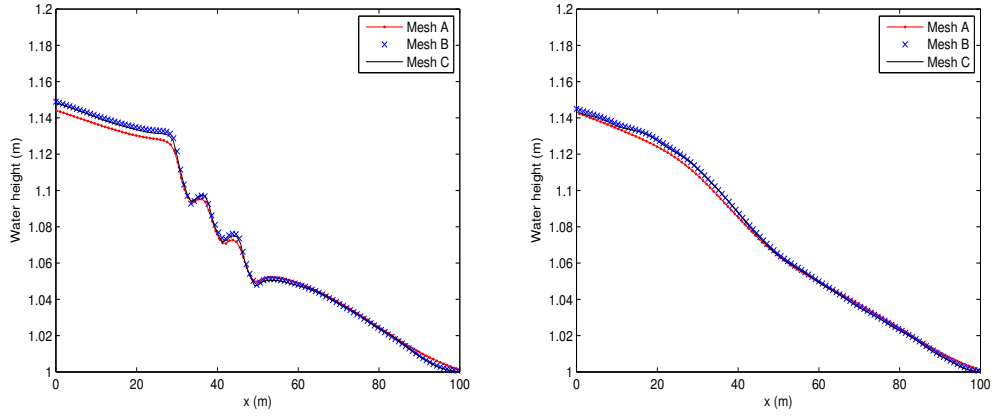
18

Figure 10. Cross-section of water height h at $y = 30\ m$ (left) and at $y = 45\ m$ (right) for the test example of shallow water flows over porous bed at time $t = 90\ s$.
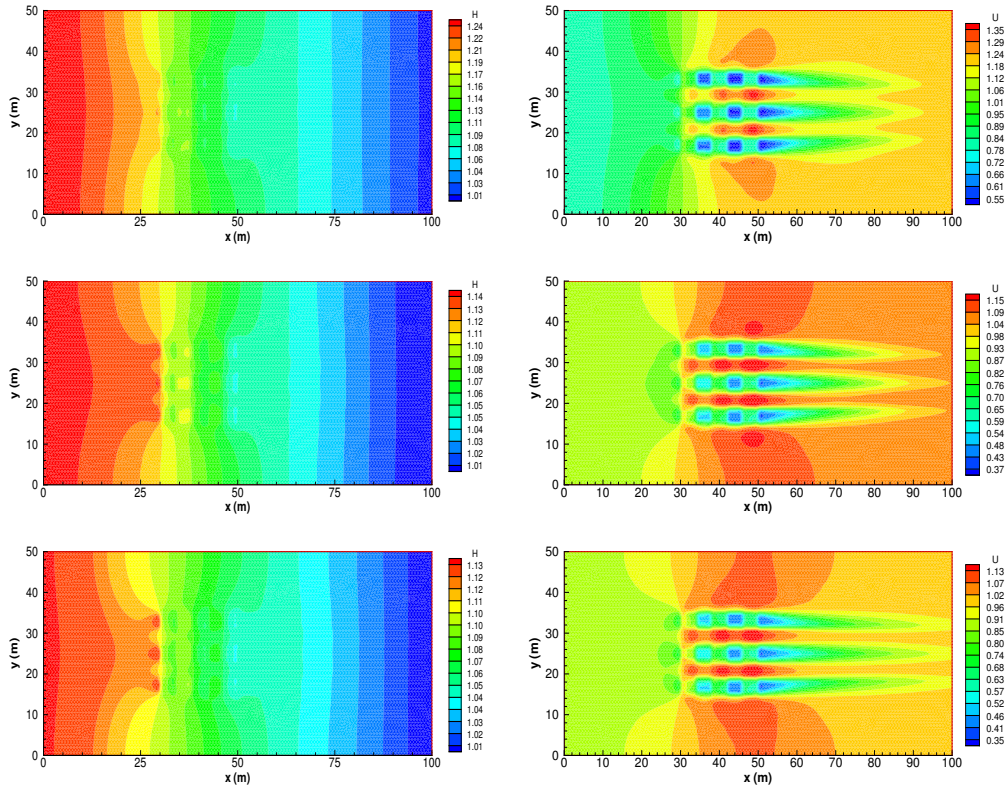

Figure 11. Snapshots of water height h (left) and water velocity u (right) for the test example of shallow water flows over porous bed at time from top to bottom $t = 60\ s$, $90\ s$ and $120\ s$.

is obtained in those regions where the gradients of the water depth are steep such as the moving fronts. Apparently, the overall flow pattern for this example is preserved with no spurious oscillations appearing in the results by the non-homogeneous Riemann solver using. Obviously, the obtained results verify the stability and the shock capturing properties of the proposed non-homogeneous Riemann solver. The proposed finite volume method performs well for this test problem since it does not diffuse the moving fronts and no spurious oscillations have been observed when the water flows over the porous media.
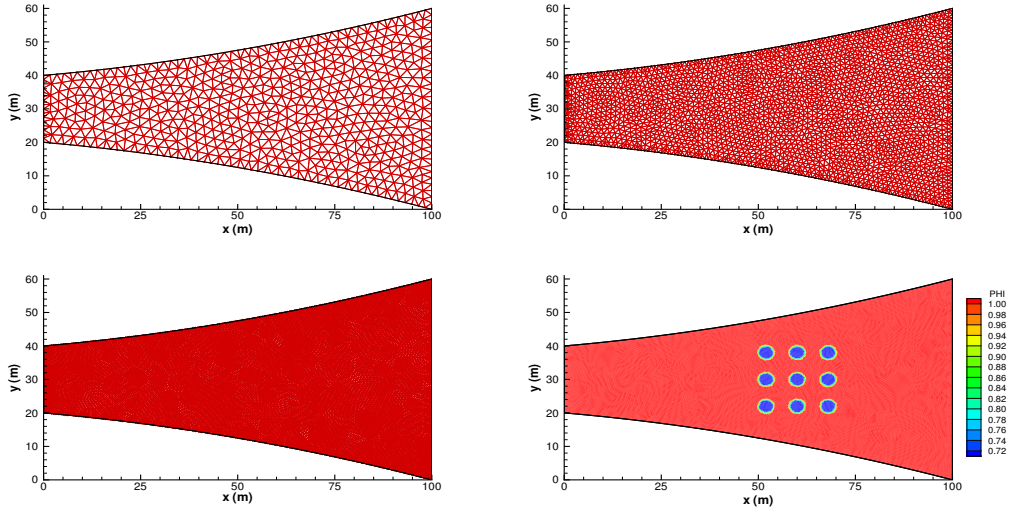
Figure 12. Meshes and porosity for the test example of complex shallow water flows over porous bed.
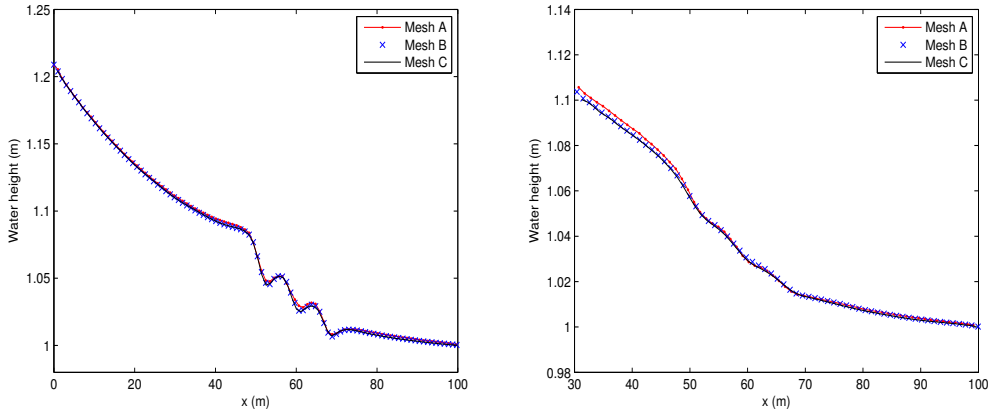

Figure 13. Cross-section of water height h at $y = 34\ m$ (left) and at $y = 44\ m$ (right) for the test example of complex shallow water flows over porous bed at time $t = 120\ s$.

4.4. *Complex shallow water flows over porous bed*

Our final test example consists on testing the performance of the proposed finite volume method for complex shallow water flows over porous bed. For this end we consider a curved channel 100 m long, 20 m wide at the entrance and 60 m wide at the exit. Similar flow domain has been studied in [15] using the standard shallow water equations. A bed slope of 0.1% is implemented in the x-direction and a constant porosity $\phi(x, y) = 1$ is assumed allover the channel except in the nine circular obstacles for which the porosity is set to $\phi(x, y) = 0.717$. The obstacles are uniformly distributed in the squared region $[50, 70] \times [20, 40]$ in the channel and the radius of each obstacle is 2 m. Compare Figure 12 for an illustration of the porosity along with the meshes used in our simulations. Initially the system is at rest and the water free-surface is set to 1 m. At the inlet boundary a total water discharge of 50 m^3/s is prescribed and on the outlet the water height of 1 m is imposed. No-slip boundary conditions are used for the remaining boundaries.

As in the previous test example we have examined the mesh convergence for this test problem of complex shallow water flows over porous bed. Three meshes namely Mesh A, Mesh B and Mesh C are used in our computations as depicted
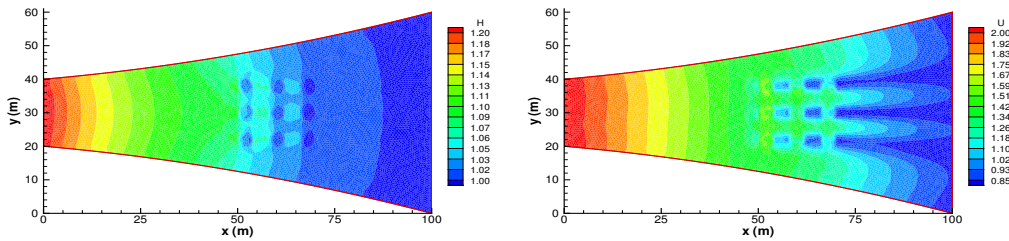
20

Figure 14. Snapshots of water height h (left) and water velocity u (right) for the test example of complex shallow water flows over porous bed at time $t = 120\ s$.

in Figure 12. The number of elements for Mesh A, Mesh B and Mesh C is 1152, 4608 and 18432 for Mesh A, Mesh B and Mesh C, respectively. The number of nodes for Mesh A, Mesh B and Mesh C is 659, 2469 and 9545, respectively. The obtained cross-sections of water height h at $y = 34\ m$ and $y = 44\ m$ at time $t = 120\ s$ are presented in Figure 13 using the three considered meshes. As can be seen from these results, a gird convergence is clearly achieved in our finite volume method as there is very little differences between the results obtained using the Mesh B and Mesh C. Similar results not reported here have also been obtained for the velocity fields. In Figure 14 we display the results for the water height h and water velocity u at time $t = 120\ s$ using the Mesh B. It is clear that the proposed finite volume method accurately solves this complex flow problem and it captures the small flow features around the circular obstacles without relying on very fine meshes. No oscillations have been detected in the water free-surface as it flows over the porous region within the channel.

5. Conclusions

In this study we have presented a class of finite volume methods for solving shallow water flows in porous media on unstructured triangular grids. The method consists of two stages which can be interpreted as a predictor-corrector procedure. In the first stage, the scheme uses the projected system of the coupled equations and introduces the sign matrix of the flux Jacobian which results in an upwind discretization of the characteristic variables. In the second stage, the solution is updated using the conservative form of the equations and a special treatment of the bed bottom in order to obtain a well-balanced discretization of the flux gradients and the source terms. Verification of the proposed method has been carried out using test problems of dam-break flows over porous media. The method exhibited good shape, high accuracy and stability behavior for all hydraulic regimes considered. The presented results demonstrate the capability of the unstructured finite volume method that can provide insight to complex shallow water flows in porous media.

An extension of the proposed finite volume to coupled models of shallow water flows in porous media and bedload transport in viscous shallow water flows will be the topic of future research. The diffusion effects and tidal waves can be important in many coastal scenarios. Another planned activity will consist in development of mesh adaptation techniques for the solution of shallow water equations with porosity. We should also emphasize that the proposed finite volume method in its current presentation does not solve shallow water flows over dry areas. To deal with such applications one has to modify the non-homogeneous Riemann solver at the predictor stage and a threshold should be added to the entries of the sign matrix

wherever they vanish. This perturbation is needed to treat dry control volumes in the computational domain.

References

[1] M.B. Abbott. *Computational hydraulics. Elements of the theory of free surface flows.* Fearon-Pitman Publishers, London, 1979.

[2] F. Benkhaldoun, I. Elmahi, and M. Seaid. Well-balanced finite volume schemes for pollutant transport by shallow water equations on unstructured meshes. *J. Comp. Physics.*, 226:180–203, 2007.

[3] F. Benkhaldoun, I. Elmahi, and M. Seaid. A new finite volume method for flux-gradient and source-term balancing in shallow water equations. *Computer Methods in Applied Mechanics and Engineering*, 199:49–52, 2010.

[4] F. Benkhaldoun, S. Sahmim, and M. Seaid. Solution of the sediment transport equations using a finite volume method based on sign matrix. *SIAM J. Sci. Comp.*, 31:2866–2889, 2009.

[5] F. Benkhaldoun, S. Sahmim, and M. Seaid. A two-dimensional finite volume morphodynamic model on unstructured triangular grids. *Int. J. Num. Meth. Fluids*, 63:1296–1327, 2010.

[6] A. Bermúdez and M.E. Vázquez. Upwind methods for hyperbolic conservation laws with source terms. *Comput. Fluids.*, 23:1049–1071, 1994.

[7] L. Cea and M.E. Vázquez-Cendón. Unstructured finite volume discretization of two-dimensional depth-averaged shallow water equations with porosity. *Int. J. Numer. Meth. Fluids*, 63:903–930, 2010.

[8] M. El-Amrani and M. Seaid. An essentially non-oscillatory semi-Lagrangian method for tidal flow simulations. *International Journal for Numerical Methods in Engineering*, 81:805–834, 2010.

[9] P. Finaud-Guyot, C. Delenne, J. Lhomme, V. Guinot, and C. Llovel. An approximate-state riemann solver for the two-dimensional shallow water equations with porosity. *Int. J. Numer. Meth. Fluids*, 62:1299–1331, 2010.

[10] V. Guinot. Multiple porosity shallow water models for macroscopic modelling of urban floods. *Advances in Water Resources*, 37:40–72, 2012.

[11] V. Guinot and S. Soares-Fraz ao. Flux and source term discretization in two-dimensional shallow water models with porosity on unstructured grids. *Int. J. Numer. Meth. Fluids*, 50:309–345, 2006.

[12] J. Hou, Q. Liang, F. Simons, and R. Hinkelmann. A 2d well-balanced shallow flow model for unstructured grids with novel slope source treatment. *Advances in Water Resources*, 52:107–131, 2013.

[13] B. Kim, B.F. Sanders, J.S. Famiglietti, and V. Guinot. Urban flood modeling with porous shallow-water equations: A case study of model errors in the presence of anisotropic porosity. *Journal of Hydrology*, 523:680–692, 2015.

[14] K. Mohamed. A finite volume method for numerical simulation of shallow water models with porosity. *Computers & Fluids*, 104:9–19, 2014.

[15] L.A. Monthe, F. Benkhaldoun, and I. Elmahi. Positivity preserving finite volume roe schemes for transport-diffusion equations. *Comput. Methods Appl. Mech. Engrg.*, 178:215–232, 1999.

[16] J. LeVeque Randall. *Numerical Methods for Conservation Laws.* Lectures in Mathematics, ETH Zürich, 1992.

[17] P.L. Roe. Approximate riemann solvers, parameter vectors and difference schemes. *J. Comp. Physics*, 43:357–372, 1981.

[18] S. Sahmim, F. Benkhaldoun, and F. Alcrudo. A sign matrix based scheme for quasi-hyperbolic non-homogeneous pdes with an analysis of the convergence stagnation problem. *J. Comput. Phys.*, 226:1753–1783, 2007.

[19] B.F. Sanders, J.E. Schubert, and H.A. Gallegos. Integral formulation of shallow-water

equations with anisotropic porosity for urban flood modeling. *Journal of Hydrology*, 362:19–38, 2008.

[20] R.L. Soulsby. *Dynamics of marine sands, a manual for practical applications.* HR Wallingford, Report SR 466, 1997.

[21] M.E. Vázquez. Improved treatment of source terms in upwind schemes for the shallow water equations in channels with irregular geometry. *J. Comp. Physics*, 148:497–526, 1999.

[22] Z. Wang and Y. Geng. Multiple porosity shallow water models for macroscopic modelling of urban floods. *Advances in Water Resources*, 37:40–72, 2012.

[23] Z. Wang and Y. Geng. Two-dimensional shallow water equations with porosity and their numerical scheme on unstructured grids. *Water Science and Engineering*, 6:91–105, 2013.